change the fracture criterion of the rock by increasing the pore pressure and/or create new cracks through hydraulic fracturing. Therefore, tremor activity with a long duration time might be caused by a chain reaction of small fractures caused by the supercritical fluid. If the condition of the tremor generation is unstable, the additional supply of fluid to an almost saturated system, or stimulation by nearby earthquake shaking, might be able to trigger the observed tremor.

References and Notes

1. B. Chouet, *Nature* **380**, 309 (1996).
2. B. R. Julian, *J. Geophys. Res.* **99**, 11859 (1994).
3. NIED Hi-net is a newly established seismic network (*10*). Each station consists of a three-component velocity seismometer with a natural frequency of 1 Hz installed at the bottom of a borehole with a depth of 100 to 200 m. The data are digitized at each station with a sampling frequency of 100 Hz, and then the data packets attached with the absolute time information from a Global Positioning System clock are transmitted to the data center.
4. Vertical-component waveforms for a pair of stations are converted to envelopes with a frequency range of higher than 4 Hz and with a smoothing time of 10 s, and they are resampled with a sampling interval of 1 s. A pair of envelope seismograms with a length of 2 min is used for calculation of the cross-correlation coefficient by moving a trace with the time lag of every 1 s to another fixed reference trace. The time lag, which gives the maximum correlation coefficient, should be the difference of the arrival time for a coherent seismic signal in the selected 2 min observed in the two stations. If the maximum correlation coefficient is less than 0.9, the time lag is not applied for the further process because there is no coherent signal. Such a correlation process is carried out for all pairs of stations in the target area. The measured time lags with a good correlation are averaged spatially to calculate the distribution of the relative arrival time like the net adjustment, which is used in the geodetic survey. The cross-correlation analysis is carried out with the moving time window of 1 min; therefore, we can calculate the location of tremors once every 1 min, continuously.
5. A. Katsumata, N. Kamaya, *Seismol. Soc. Jpn. Fall Meeting* B16 (2001).
6. M. Ukawa, K. Obara, *Bull. Volcanol. Soc. Jpn.* **38**, 187 (1993).
7. A. Hasegawa, A. Yamamoto, *Tectonophysics* **233**, 233 (1994).
8. S. Ohmi, *Eos* **82** (fall suppl.), 871 (2001).
9. H. Bureayu, H. Keppler, *Earth Planet. Sci. Lett.* **165**, 187 (1999).
10. K. Obara *et al.*, *Eos* **81** (fall suppl.), 863 (2000).
11. M. Nakamura *et al.*, *Ann. Disaster Prev. Res. Inst. Kyoto* **40 B-1**, 1 (1997).

30 January 2002; accepted 11 April 2002

Microscopic View of Structural Phase Transitions Induced by Shock Waves

Kai Kadau,[1,2]* Timothy C. Germann,[3] Peter S. Lomdahl,[1] Brad Lee Holian[1]

Multimillion-atom molecular-dynamics simulations are used to investigate the shock-induced phase transformation of solid iron. Above a critical shock strength, many small close-packed grains nucleate in the shock-compressed body-centered cubic crystal growing on a picosecond time scale to form larger, energetically favored grains. A split two-wave shock structure is observed immediately above this threshold, with an elastic precursor ahead of the lagging transformation wave. For even higher shock strengths, a single, overdriven wave is obtained. The dynamics and orientation of the developing close-packed grains depend on the shock strength and especially on the crystallographic shock direction. Orientational relations between the unshocked and shocked regions are similar to those found for the temperature-driven martensitic transformation in iron and its alloys.

Since the ancient Greeks, the structural transformation in steel has been used to harden swords by rapid cooling. The underlying physics was first seriously explored by Martens in the late 19th century, and, because of his work, the diffusionless structural phase transitions in steel and other materials have become known as martensitic transformations (*1*, *2*). Concomitant effects, such as the aforementioned hardening, pseudoelastic, and shape memory effects, are used to design special materials for medical and engineering applications (*1*, *2*). Structural transformations are also observed in biological systems, as some virus species use the pressure-induced martensitic transformation to infect bacteria cells (*3*).

Despite this great importance in technology and nature, many open questions remain, mostly related to the underlying atomistic processes. Martensitic transformations are characterized by a collective movement of atoms across distances that are typically smaller than one nearest-neighbor spacing. Crystallographic orientational relations between the two phases exist, and the resulting crystal exhibits fine-scale inhomogeneities such as slip, twinning, and stacking faults. The best known martensitic transformation is that of Fe and its alloys; for example, Fe/Ni alloys transform on cooling from a high-temperature face-centered cubic (fcc) phase to a low-temperature body-centered cubic (bcc) phase. Other examples are alloys based on CuAl, NiTi, NiAl, and ceramics like ZrO_2 (*2*), to name only a few. All these transformations are first order, which means they exhibit hysteresis and can be overheated or undercooled like the fluid-solid transition of water. The temperature and the height of the energy barrier between the two phases determine whether the transformation is induced by thermal fluctuations (homogeneous nucleation) or by preexisting defects, which locally reduce the energy barrier and act as nucleation centers (heterogeneous nucleation).

Such structural transformations can be caused by either temperature or pressure changes. Shock waves lead to increases in both pressure and temperature, inducing a close-packed structure due to a martensitic-like transformation (*4*, *5*). Ab initio electronic structure calculations (*6*) and molecular-dynamics simulations (*7*) are appropriate methods for atomic-scale investigations of these phenomena. Whereas ab initio methods are limited to very small system sizes, large-scale molecular-dynamics (MD) simulations using empirical potentials give insight into the motion of millions of atoms on the pico- and nanosecond time scale for a variety of physical problems, including crack propagation (*8*, *9*), friction (*10*–*12*), dislocation dynamics (*13*, *14*), shock waves (*15*, *16*), and structural phase transitions (*17*–*21*).

Here, we report the investigation of shock-induced structural phase transitions using massively parallel MD simulations (*22*). Simulations were carried out for two different embedded-atom method (EAM) potentials (*23*) describing the forces between the atoms in a metal (*24*). Shock waves were initiated by a "momentum mirror" (*15*), which specularly reflects any atoms reaching the face of a perfectly flat, infinitely massive piston moving at the piston (or particle) velocity u_p (*25*). The resulting shock wave moves in front of the piston at the shock velocity u_s. To minimize surface and edge effects, periodic boundary conditions perpendicular to the shock direction are applied, simulating a pseudoinfinite lateral dimension. Shock waves were generated in both the [001] and [011] directions of an initially perfect bcc

[1]Theoretical Division, Los Alamos National Laboratory, Los Alamos, NM 87545, USA. [2]Theoretische Tieftemperaturphysik, Gerhard-Mercator-Universität Duisburg, Lotharstraße 1, 47048 Duisburg, Germany. [3]Applied Physics Division, Los Alamos National Laboratory, Los Alamos, NM 87545, USA.

*To whom correspondence should be addressed: E-mail: kkadau@lanl.gov

single crystal; for clarity and brevity, we will focus on the [001] results.

For low piston velocities, an elastic shock wave uniaxially compresses the sample in a reversible manner (Fig. 1A). We see no evidence for bcc plasticity before the onset of the bcc → hexagonal close-packed (hcp) phase transformation, due to the increased Hugoniot elastic limit (the threshold for elastic-plastic transition) of perfect single crystals compared with real engineering samples, which are defective and polycrystalline. In the latter, the Hugoniot elastic limit is only around 1 GPa, so that a three-wave shock structure is possible: an elastic precursor is followed by a slower plastic wave and then by an even slower phase-transformation front. Instead, for the perfect crystals studied here, we see a split two-wave shock structure: an elastic precursor is followed by a slower phase-transformation wave without any intermediate elastic-plastic transition (Movie S1; Fig. 1, B and C). Above the phase transition threshold, homogeneous nucleation of close-packed grains (Fig. 2) in the uniaxially compressed bcc matrix relaxes the shear stress behind the shock front. Near the threshold, the transformation front is rough because only a few nucleii grow and establish the front. With increasing shock strength (Fig. 1, B to D), the driving force for the structural transition increases, thus producing nucleation centers more rapidly by homogeneous nucleation (Movie S2). This results in a smoother transformation front, which at very high shock strengths (Fig. 1D) overtakes the elastic precursor, resulting in a single overdriven wave.

By carrying out simulations for various u_p and measuring the resulting shock velocity u_s (two such velocities in the special case where an elastic precursor exists), we obtain the shock adiabat, or "Hugoniot," as the locus of final shocked states (Fig. 3) (*26*, *27*). Conservation of mass and momentum across a planar shock discontinuity lead to "jump conditions" relating the initial (subscript 0) and final states (*28*):

$$V/V_0 = 1 - u_p/u_s \quad (1)$$

$$P_{zz} - P_0 = u_s u_p / V_0 \quad (2)$$

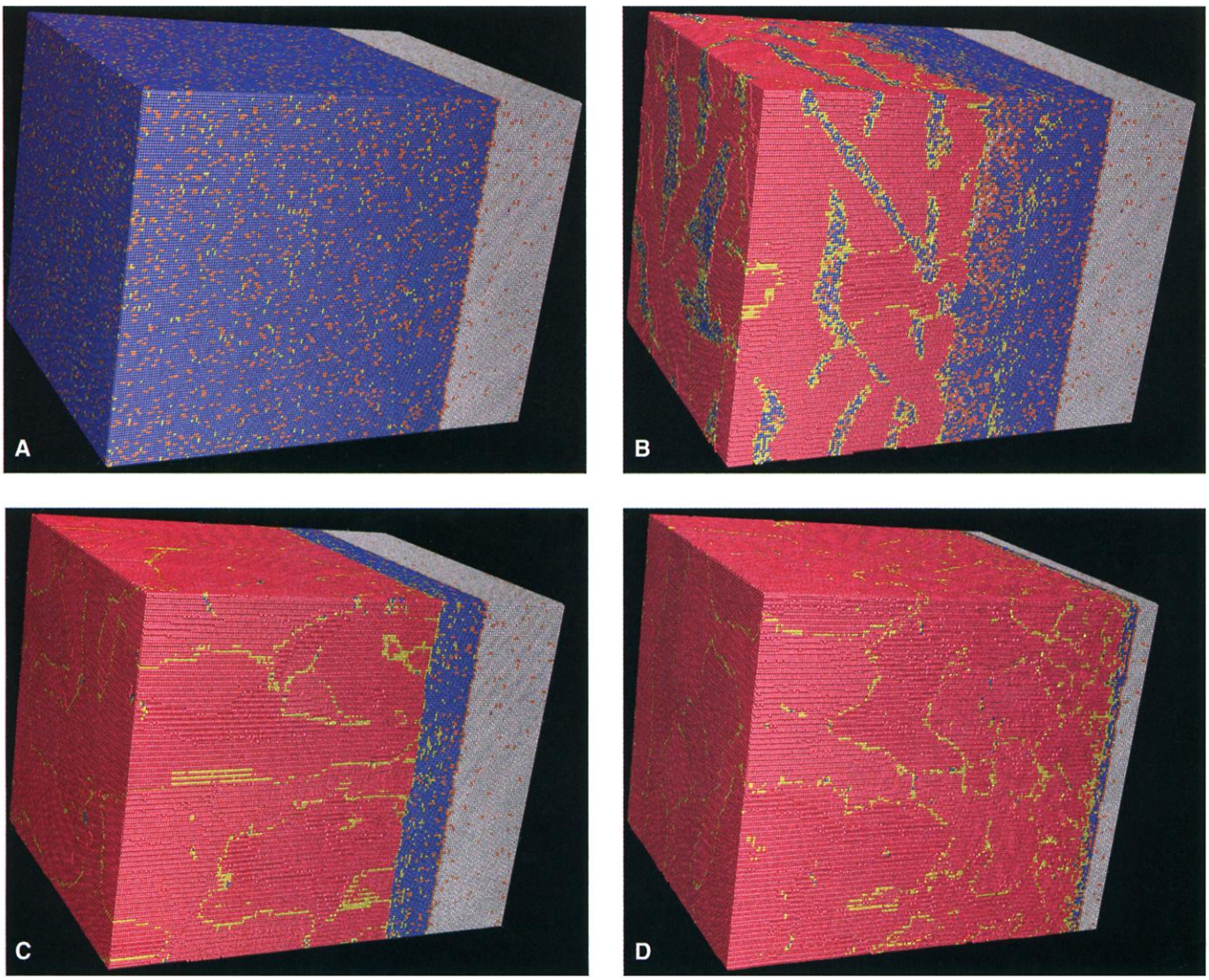

Fig. 1. Shocked samples (shock fronts propagate from left to right) after 8.76 ps for four different shock strengths in the bcc [001] direction as follows: piston velocities u_p are (**A**) 362 m/s (u_p/c_0 = 0.0731, c_0 = longitudinal sound velocity in [001] direction at zero temperature), (**B**) 471 m/s (u_p/c_0 = 0.0951), (**C**) 689 m/s (u_p/c_0 = 0.139), and (**D**) 1087 m/s (u_p/c_0 = 0.219). Atoms are color-coded by the number of neighbors n within 2.75 Å. Gray, unshocked bcc (n = 8); blue, uniaxially compressed bcc (n = 10); and red, the transformed close-packed grains (n = 12) separated by yellow (n = 11) grain boundaries. Just above the transformation threshold (B), the transformation shock front is rough and slower than the elastic precursor. This roughness and the difference between the velocities of the elastic precursor and the transformation front vanish with increasing shock strength (B to D). At larger shock strengths, the higher temperatures in the transformed region accelerate the annealing process behind the shock front, whereby initially formed small grains merge and leave only a few large grains (D).

where P_{zz} is the longitudinal pressure. Extension to multiple-wave structures is straightforward. Behind the shock front, P and ρ (density $\rho = 1/V$), as measured directly in the simulations, are in good agreement with calculated values from these jump conditions. For the Voter-Chen potential, the transition pressure of 15 GPa is in good agreement with the experimental 13 GPa (*26*, *27*) (Fig. 3). However, the Meyer-Entel potential (*29*) is much too repulsive upon compression (*30*), creating a transition pressure of 55 GPa that is much too high. Attempts to fit an EAM potential that well reproduced both the temperature-driven and the pressure-driven phase transitions failed, suggesting that the modified embedded-atom method may be required for a more global description of the iron phase diagram (*31*). This demonstrates the complexity of Fe and reveals that one must be careful in using semiempirical potentials over too wide a range of conditions. However, it is important to emphasize that, under shock loading, the two different potentials lead to the same physical processes.

Useful information on the structure behind the shock front can be obtained from the radial distribution function (*7*) (Fig. 4). The uniaxially compressed material shows, as expected, a tetragonal distortion splitting of individual neighbor peaks. However, the transformed material shows characteristic peaks corresponding to a close-packed structure. Closer analysis (Fig. 5) shows a mainly ABAB stacking sequence of close-packed planes, that is, a hcp structure with only a few ABABCB intrinsic stacking faults, in accord with experimental observations (*4*).

Analysis of the dynamics of the close-packed grains shows small grains whose diameters are a few lattice constants developing near the piston front, with grain boundaries along (110) and $(1\bar{1}0)$ planes of the bcc crystal (Fig. 2). These grains grow on a picosecond time scale, with grain boundaries extending along the $[001]_{bcc}$ shock direction, leading to a twinned hcp structure (Fig. 5). The healing of the grain boundaries behind the shock front is more pronounced with increasing shock strength and, thus, increasing temperature (Fig. 1, B to D). The ABAB-stacked (110) and $(1\bar{1}0)$ planes of the bcc crystal transform into $(0001)_{hcp}$ close-packed planes [analogous to $(111)_{fcc}$], also with a nearly perfect ABAB stacking sequence (Fig. 5). The $[110]_{bcc}$ (or $[\bar{1}10]_{bcc}$) direction transforms into the $[10\bar{1}0]_{hcp}$ direction, analogous to $[112]_{fcc}$. This crystallographic orientational relation, $(110)_{bcc} \parallel (0001)_{hcp}$ and $[110]_{bcc} \parallel [10\bar{1}0]_{hcp}$, is the hcp analog of the well-known Nishiyama-Wassermann relation that is common for many Fe alloys transforming between bcc and fcc structures (*2*). However, the situation becomes more complex for shock loading in the [011] direction. Above the transformation threshold, smaller grains are formed with more variants of the resulting close-packed phase due to different transformation mechanisms, with the $(011)_{bcc}$

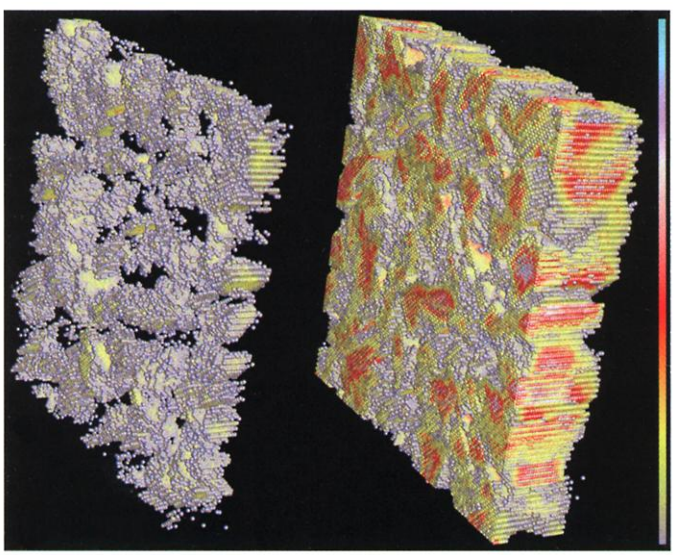

Fig. 2. Nucleation of close-packed material in the bcc matrix for a shock strength above the transformation threshold [u_p = 471 m/s, (Fig. 1B)]. Only atoms with a transverse movement above 0.42 Å are shown and colored by their transverse displacement [gray = 0.42 Å, cyan ≥ 1.32 Å (about half the nearest neighbor distance)], showing nucleation centers induced by statistical thermal fluctuations. After 1.095 ps (left), small nucleation centers start to grow along close-packed planes and finally build the transformation front (right, after 2.19 ps).

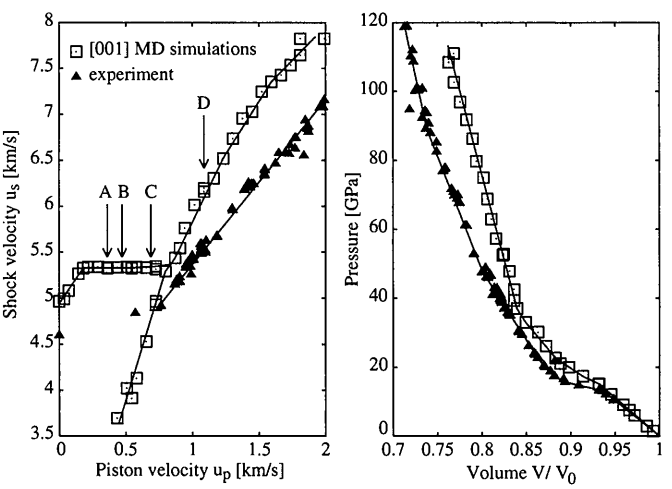

Fig. 3. Measured shock velocities u_s as a function of piston velocity u_p demonstrating the existence of split two-wave shock structure, due to a structural transition; the corresponding pressure-volume Hugoniot is obtained from the jump conditions. Triangles, experimental polycrystal data (*26*, *27*); squares, perfect single crystal MD simulations in the bcc [001] direction. The longitudinal sound velocity c_0 is the weak-shock limit corresponding to $u_p = 0$. The initial specific volume is $V_0 = 0.1273$ cm³/g. The letters A, B, C, and D correspond to the "snapshots" shown in Fig. 1. The interatomic many-body interactions were prescribed by a Voter-Chen EAM potential, which was not explicitly fitted to shockwave data (*38*).

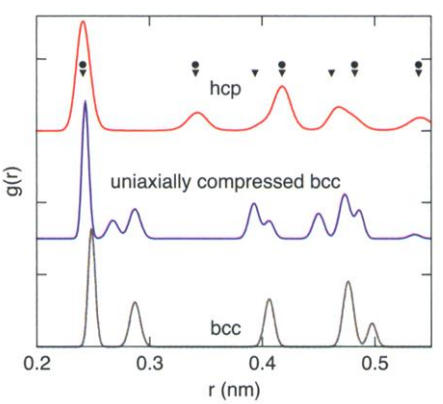

Fig. 4. Radial distribution functions of an initially perfect bcc crystal for different shock strengths. The unshocked bcc sample (gray) clearly shows the eight nearest and six next-nearest neighbors close together. The elastically shocked (uniaxially compressed) bcc crystal (blue) shows the splitting of individual neighbor peaks due to tetragonal distortion. At larger shock strength, the structural transformation from bcc to the close-packed hcp structure (red) is visible. (Thermal broadening of the peaks increases with increasing shock strength as well.) Triangles and circles refer to ideal neighbor shells of hcp and fcc crystals, respectively. The small left shoulder and the larger right shoulder of the third and fourth peak of the red curve reflect that the third and fourth neighbor shells of the hcp lattice consist of 2 and 18 atoms, respectively, whereas the fifth and sixth shells possess 12 and 6 atoms, respectively.

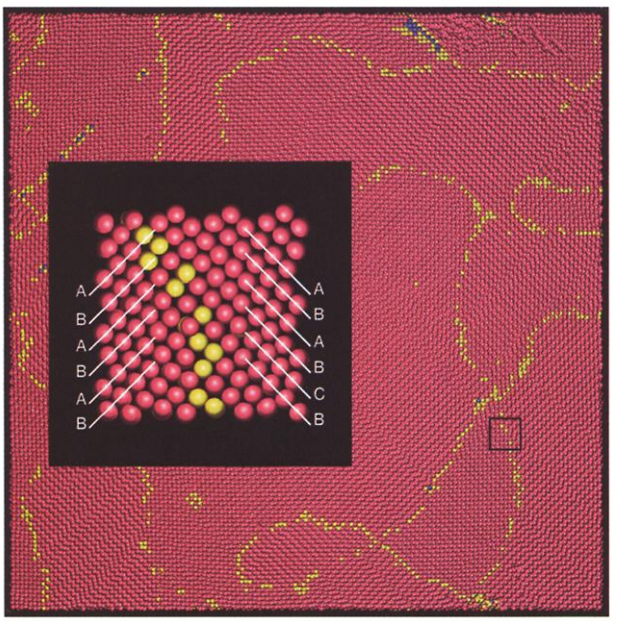

Fig. 5. Cross section (edge length = 40.2 nm) near the piston front of the sample shown in Fig. 1D. Twinned close-packed crystals (n = 12, red spheres) are evident, separated by a pattern of low-coordination (n = 11, yellow spheres or n = 10, blue spheres) grain boundaries. The close-packed planes of the initial bcc structure transform to the close-packed planes of the nearly perfect hcp structure. The inset shows twinned close-packed grains separated by a twin boundary. (The inset shows the spheres with a smaller radius in order to demonstrate the packing of the planes more clearly.) The stacking sequence of the close-packed planes indicates a nearly perfect hcp structure (ABAB), with one stacking fault (ABCB) on the right side.

plane transforming to either square [as in $(001)_{fcc}$] or hexagonal [as in $(111)_{fcc}$] planes.

Because common bulk iron is polycrystalline, existing experimental data such as those shown in Fig. 3 are complicated by two factors: the distribution of grain orientations and the presence of grain boundaries that can serve as heterogeneous nucleation sites. The perfect crystal simulations presented here must rely on the slower homogeneous nucleation process, but preliminary simulations in which an extended defect is present have confirmed that the transformation threshold is reduced when heterogeneous nucleation sites exist, an effect also found for the plastic threshold in fcc crystals (*15*).

Ultrafast time-resolved laser-generated x-ray diffraction (*32*) studies of single crystals subjected to laser-induced shocks are being planned to confirm these findings. Dynamic x-ray diffraction spectra—both shifts in peaks and broadenings—can be obtained from our simulations for direct comparison with results from in situ experiments done while the shock wave is in progress.

The techniques we have demonstrated in this paper are universal and applicable to a large class of problems in materials science where the dynamics of phase changes are important. Future atomistic simulation work, building on the foundations laid in this paper, may encompass even higher pressure phase changes in iron that are of great current interest to the geophysics community.

References and Notes

1. C. M. Wayman, H. K. D. H. Bhadeshia, in *Physical Metallurgy*, R. W. Cahn, P. Haasen, Eds. (North-Holland, Amsterdam, 1996), vol. 2, chap. 15.
2. L. Delaey, in *Phase Transformations in Materials*, R. W. Cahn, P. Haasen, E. J. Kramer, Eds. (VCH, Weinheim, Germany, 1991), vol. 5, pp. 339–404.
3. H. Czichos, in *The Martensitic Transformation in Science and Technology*, E. Hornbogen, N. Jost, Eds. (DGM Informationsgesellschaft, Oberursel, Germany, 1989), chap. 1.
4. G. E. Duvall, R. A. Graham, *Rev. Mod. Phys.* **49**, 523 (1977).
5. M. A. Meyers, *Dynamic Behavior of Materials* (Wiley-Interscience, New York, 1994), chap. 8.
6. J. Kübler, V. Eyert, in *Electronic Structure and Magnetic Properties of Metals and Ceramics, Part I*, K. H. J. Buschow, Ed. (VCH, Weinheim, Germany, 1994), vol. 3A, chap. 1.
7. D. C. Rapaport, *The Art of Molecular Dynamics Simulation* (Cambridge Univ. Press, Cambridge, 1995).
8. S. J. Zhou, D. M. Beazley, P. S. Lomdahl, B. L. Holian, *Phys. Rev. Lett.* **78**, 479 (1997).
9. M. Marder, *Comput. Sci. Eng.* **1**, 48 (1999).
10. M. Cieplak, E. D. Smith, M. O. Robbins, *Science* **265**, 1209 (1994).
11. B. Bhushan, J. N. Israelachivili, U. Landman, *Nature* **374**, 607 (1995).
12. B. L. Holian, J. E. Hammerberg, P. S. Lomdahl, *J. Comput. Aided Mater. Design* **5**, 207 (1998).
13. S. J. Zhou, D. L. Preston, P. S. Lomdahl, D. M. Beazley, *Science* **279**, 1525 (1998).
14. P. Gumbsch, H. Gao, *Science* **283**, 965 (1999).
15. B. L. Holian, P. S. Lomdahl, *Science* **280**, 2085 (1998).
16. T. C. Germann, B. L. Holian, P. S. Lomdahl, R. Ravelo, *Phys. Rev. Lett.* **84**, 5351 (2000).
17. S. Rubini, P. Ballone, *Phys. Rev. B* **48**, 99 (1993).
18. Y. Shao, P. C. Clapp, J. A. Rifkin, *Met. Mater. Trans. A* **27**, 1477 (1996).
19. F. Shimojo, I. Ebbsjö, R. K. Kalia, A. Nakano, J. P. Rino, P. Vashishta, *Phys. Rev. Lett.* **84**, 3338 (2000).
20. P. Entel, K. Kadau, R. Meyer, H. C. Herper, M. Schröter, E. Hoffmann, *Phase Transitions* **65**, 79 (1999).
21. K. Kadau, P. Entel, T. C. Germann, P. S. Lomdahl, B. L. Holian, *J. Phys. IV (Paris)*, **11**, Pr8-17 (2001).
22. We used the high-performance parallel molecular-dynamics code SPaSM (*33–35*) to routinely simulate about 8 million atoms, that is, samples with dimensions of 40.2 nm × 40.2 nm × 57.4 nm (Fig. 1), on a 12-processor shared-memory Sun Enterprise 4000. A few additional simulations with 25 million atoms were carried out using 64 nodes of the Avalon Alpha/Linux cluster at Los Alamos (*36*, *37*).
23. M. S. Daw, S. M. Foiles, M. I. Baskes, *Mater. Sci. Rep.* **9**, 251 (1993).
24. A specific EAM potential for Fe/Ni alloys that describes essential properties such as the lattice constant, cohesive energy, elastic constants, vacancy formation energy, and phonon frequencies (*29*) was previously used to study the fcc ↔ bcc temperature-driven transformation (*20*). Here, we used this many-body potential and a Voter-Chen EAM Fe potential (*38*), which better represents high-pressure experiments even though it was not fitted to them (*30*). The qualitative behavior of the shock-induced phase transformation for both EAM potentials is quite similar. Other potentials for Fe have been proposed for higher pressure regimes (*39–41*) but were deemed not appropriate for this study; for example, the first two do not have a bcc ground state at zero pressure and temperature.
25. For computational convenience, a piston-centered frame of reference is employed so that the sample is initially traveling at a z velocity $-u_p$ toward a fixed piston at z = 0.
26. R. G. McQueen, S. P. Marsh, J. W. Taylor, J. N. Fritz, W. J. Carter, in *High-Velocity Impact Phenomena*, R. Kinslow, Ed. (Academic, New York, 1970), pp. 293–417.
27. J. M. Brown, J. N. Fritz, R. S. Hixson, *J. Appl. Phys.* **88**, 5496 (2000).
28. Conservation of energy across the shock front leads to a third jump condition that is not needed for the present work. Temperatures, if desired, can be directly computed from the particle velocities in our MD simulations, without any assumptions about the equation of state.
29. R. Meyer, P. Entel, *Phys. Rev. B* **57**, 5140 (1998).
30. The importance of properly accounting for anharmonicity, e.g., by requiring that the potential obey a reasonable equation of state (*42*) under uniform compression and dilation, has been pointed out (*43*).
31. M. I. Baskes, *Phys. Rev. B* **46**, 2727 (1992).
32. A. Loveridge-Smith *et al.*, *Phys. Rev. Lett.* **86**, 2349 (2001).
33. P. S. Lomdahl, P. Tamayo, N. Grønbech-Jensen, D. M. Beazley, in *Proceedings of Supercomputing 93*, G. S. Ansell, Ed. (IEEE Computer Society Press, Los Alamitos, CA, 1993), pp. 520–527.
34. D. M. Beazley, P. S. Lomdahl, *Computers in Physics* **11**, 230 (1997).
35. For more information about SPaSM, see http://bifrost.lanl.gov/MD/MD.html.
36. M. S. Warren, T. C. Germann, P. S. Lomdahl, D. M. Beazley, J. K. Salmon, on *Proceedings of the 1998 ACM / IEEE SC98 Conference* CD-ROM (IEEE Computer Society, 1998).
37. Please see http://cnls.lanl.gov/avalon/ to review the work of the Avalon group at Los Alamos.
38. R. J. Harrison, A. F. Voter, S.-P. Chen, in *Atomistic Simulation of Materials Beyond Pair Potentials*, V. Vitek, D. J. Srolovitz, Eds. (Plenum Press, New York, 1989), p. 219.
39. M. Matsui, O. L. Anderson, *Phys. Earth Planet. Inter.* **103**, 55 (1997).
40. R. E. Cohen, L. Stixrude, E. Wassermann, *Phys. Rev. B* **56**, 8575 (1997).
41. B. Belonoshko, R. Ahuja, *Phys. Earth Planet. Inter.* **102**, 171 (1997).
42. J. H. Rose, J. R. Smith, F. Guinea, J. Ferrante, *Phys. Rev. B* **29**, 2963 (1984).
43. S. M. Foiles, M. S. Daw, *Phys. Rev. B* **38**, 12643 (1988).

44. K.K. would like to thank P. Entel and R. Meyer (Duisburg) for many helpful discussions and support. This work has been supported by the DOE under contract nos. W-7405-ENG-36 and LDRD-DR 2001501 and by the German science council (Deutsche Forschungsgemeinschaft) through the Graduate College "Structure and Dynamics of Heterogeneous Systems" and SFB 445. It is also a pleasure to thank our colleagues S. Grabowski, J. Hammerberg, R. Ravelo, and J. S. Wark.

Supporting Online Material

www.sciencemag.org/cgi/content/full/296/5573/1681/DC1
Materials and Methods
Movies S1 and S2

30 January 2002; accepted 12 April 2002